Airborne spectral measurements of surface–atmosphere anisotropy for several surfaces and ecosystems over southern Africa

Charles K. Gatebe,[1,2] Michael D. King,[2] Steve Platnick,[2] G. Thomas Arnold,[2,3] Eric F. Vermote,[2,4] and Beat Schmid[5,6]

[1] The Cloud Absorption Radiometer (CAR) was flown aboard the University of Washington Convair CV-580 research aircraft during the Southern Africa Regional Science Initiative 2000 (SAFARI 2000) dry season campaign and obtained measurements of bidirectional reflectance distribution function (BRDF) for a variety of natural surfaces and ecosystems in southern Africa. To measure the BRDF of the surface–atmosphere system, the University of Washington CV-580 banked at a roll angle of ∼20° and flew circles about 3 km in diameter above the surface, taking approximately 2 min. Multiple circular orbits were acquired over selected surfaces so that average BRDFs could be acquired, smoothing out small-scale surface and atmospheric inhomogeneities. In this paper, we present results of BRDFs taken over two Earth Observing System (EOS) validation sites: Skukuza tower, South Africa (25.0°S, 31.5°E) and Mongu tower, Zambia (15.4°S, 23.3°E). Additional sites are discussed and include the Maun tower, Botswana (20.0°S, 23.6°E), Sua Pan, Botswana (20.6°S, 25.9°E), Etosha Pan, Namibia (19.0°S, 16.0°E), and marine stratocumulus clouds off the west coast of Namibia (20.5°S, 13.1°E). Results clearly show anisotropy in reflected solar radiation over the various surfaces types: savanna, salt pans, and cloud. The greatest anisotropy is observed over marine stratus clouds, which exhibit strong forward scattering as well as important water cloud scattering features such as the rainbow and glory. The BRDF over savanna is characterized by a distinct backscattering peak in the principal plane and shows directional and spectral variations. Over the pans, the BRDF is more enhanced in the backscattering plane than forward scattering plane and shows little directional variation. *INDEX TERMS:* 0315 Atmospheric Composition and Structure: Biosphere/atmosphere interactions; 1640 Global Change: Remote sensing; 1694 Global Change: Instruments and techniques; 9305 Information Related to Geographic Region: Africa; 3359 Meteorology and Atmospheric Dynamics: Radiative processes; 3360 Meteorology and Atmospheric Dynamics: Remote sensing; *KEYWORDS:* BRDF, SAFARI 2000, surface reflectance, airborne measurements, radiometer, multispectral

1. Introduction

[2] This paper discusses measurements of surface anisotropy for different surfaces and ecosystems in southern Africa obtained with NASA's Cloud Absorption Radiometer (CAR) aboard the University of Washington Convair CV-

580 research aircraft. The measurements were obtained during the Southern Africa Regional Science Initiative 2000 (SAFARI 2000) dry season campaign between 10 August and 18 September 2000 [*Swap et al.*, 2002].

[3] The properties of anisotropically scattering surfaces in the reflection of solar incident light is described and specified by the bidirectional reflectance distribution function (BRDF). The BRDF provides a way of geometrically and quantitatively expressing the connection between radiance reflected from a location into a given direction and the incident irradiance at that location arriving from some other direction (including, in the case of retroreflection, the same direction) [*Nicodemus et al.*, 1977]. The BRDF is needed in remote sensing for the correction of view and illumination angle effects, for example, in image standardization and mosaicing [*Wu et al.*, 1995; *Li et al.*, 1996; *Strahler et al.*, 1996a]. It is also needed for deriving surface albedo [*Wanner et al.*, 1995; *Lewis*, 1995; *Strahler et al.*, 1996b;

[1]Goddard Earth Science and Technology Center, University of Maryland Baltimore County, Baltimore, Maryland, USA.
[2]Earth Sciences Directorate, National Aeronautics and Space Administration (NASA) Goddard Space Flight Center, Greenbelt, Maryland, USA.
[3]L3 Communications—EER Communications Systems, Inc., Chantilly, Virginia, USA.
[4]Department of Geography, University of Maryland, College Park, Maryland, USA.
[5]Bay Area Environmental Research Institute, Sonoma, California, USA.
[6]NASA Ames Research Center, Moffett Field, California, USA.
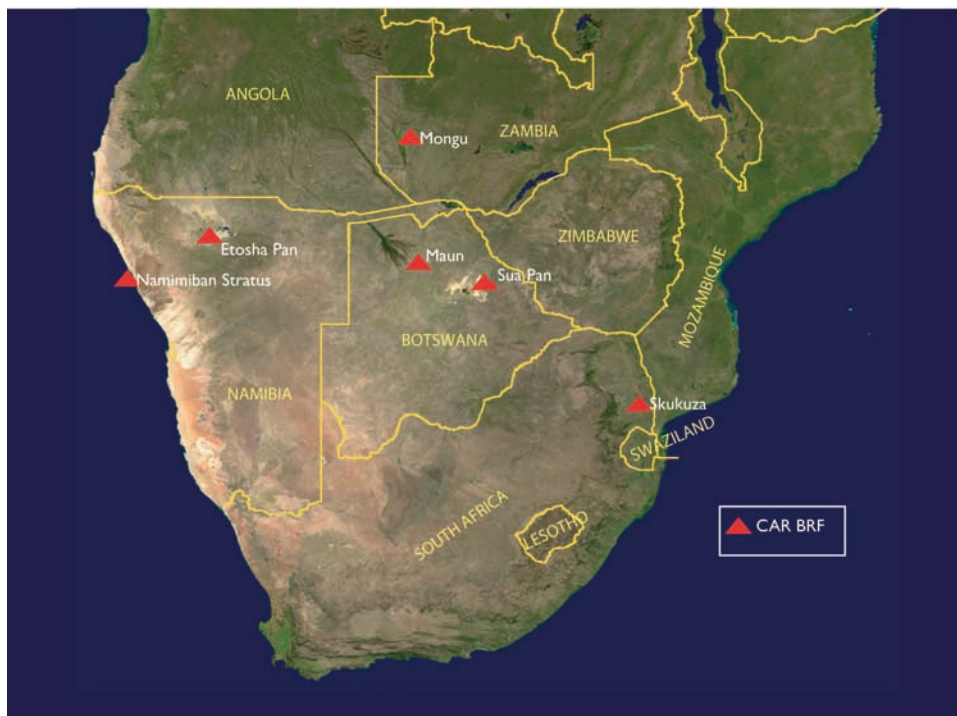
Figure 1. Locations of airborne measurements of BRDF obtained during the SAFARI 2000 field experiment from 12 August to 16 September 2000 using NASA's CAR. The background image on which the BRDF locations are mapped is a color composite of MODIS surface reflectance produced from atmospherically corrected 8-day MODIS reflectance data product.

Leroy et al., 1997]. Since albedo is an angular-weighted integration of reflection function over a hemisphere, the acquisition of radiometric measurements at different angles may improve its accuracy [cf. *Kimes et al.*, 1987]. Accurate albedo measurements are not only important for assessing the role of albedo in energy balance schemes [*Kustas et al.*, 1989] but are also important for accurate weather and climate modeling [e.g., *Dickinson et al.*, 1990; *Lean and Rowntree*, 1997]. Some studies have shown that the BRDF can be used to improve land cover classification [*Cihlar et al.*, 1994; *Gutman*, 1994; *Moody and Strahler*, 1994; *Wu et al.*, 1995], for cloud detection [*DiGirolamo and Davies*, 1994; *d'Entremont et al.*, 1996; *Leroy et al.*, 1997], and for atmospheric correction [*Kaufman*, 1989]. This underpins the importance of BRDF measurements, a fact recognized more than three decades ago [*Salomonson and Marlatt*, 1968, 1971].

[4] The CAR [*King et al.*, 1986] flying aboard the University of Washington aircraft has provided a convenient and efficient means of obtaining complete BRDFs for several surfaces types at a landscape level. Figure 1 shows the location of all sites for which CAR BRDF measurements were obtained throughout the SAFARI 2000 dry season campaign. In addition to these observations, CAR BRDF measurements have previously been obtained of a smoke layer from the Kuwait oil fires at 0.75 and 1.64 μm [*King*, 1992], cerrado, dense forest, and smoke from forest fires in Brazil [*Tsay et al.*, 1998], the Saudi Arabian desert, forested wetland (Great Dismal Swamp), and ocean water containing Sun glint over the

Atlantic Ocean and the Persian Gulf [*Soulen et al.*, 2000], and four common arctic surfaces (snow-covered sea ice, melt-season ice, snow-covered tundra, and tundra shortly after snowmelt) [*Arnold et al.*, 2002]. In this paper, we discuss BRDF measurements of various surfaces throughout southern Africa, including savanna, salt pans, and marine stratocumulus clouds off the coast of Namibia. More importantly, this paper examines the sensitivity of atmospheric correction to errors in aerosol optical depth and its angular dependence.

[5] The remainder of this paper is organized into four sections. Section 2, the theory, discusses the principal approach and formulation used to compute BRDF, while section 3 focuses on the instrument, calibration, BRDF measurement method, and atmospheric correction. Section 4 presents our results of the spectral BRDF and is thematically arranged to reflect similarities of the surfaces types: savanna, salt pans, and clouds. Section 5 concludes with a summary of the study.

2. Theory

[6] The bidirectional reflectance distribution function (BRDF) gives the reflectance of a target as a function of illumination geometry and viewing geometry, hence carries information about the anisotropy of the surface. It depends on wavelength and is determined by the structural and optical properties of the surface, such as shadow-casting, multiple scattering, mutual shadowing, transmission, reflection and absorption by surface element facet orienta-
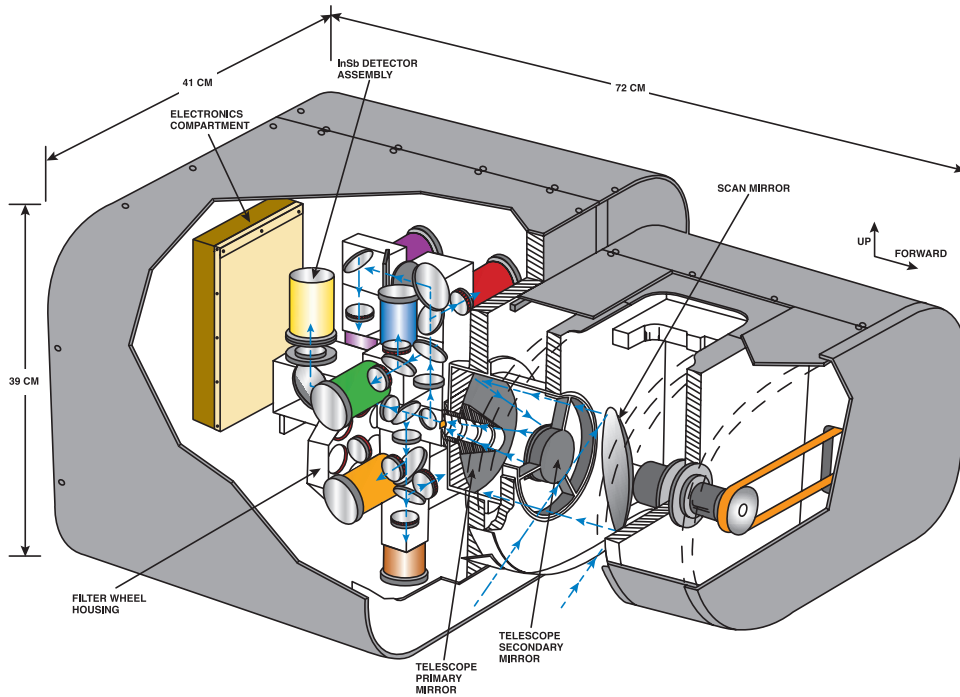
Figure 2. Cutaway drawing of the CAR. The instrument housing is approximately 72 cm long, 41 cm wide, and 39 cm deep and weighs 42 kg. The CAR has 14 narrow spectral bands between 0.34 and 2.30 μm. The CAR images the sky and surface at an IFOV of ~1° through any plane defined by 190°. Modified from the study of *King et al.* [1986].

tion distribution and density. BRDF is needed in remote sensing for the correction of view and illumination angle effects (for example in image standardization and mosaicing), for deriving albedo, for land cover classification, for cloud detection, for atmospheric correction, and other applications. It gives the lower radiometric boundary condition for any radiative transfer problem in the atmosphere and is hence of relevance for climate modeling and energy budget investigations.

[7] We prefer to express the spectral BRDF (R_λ) following *van de Hulst*'s [1980] formulation:

$$\mathbf{R}_\lambda(\theta, \theta_0, \phi) = \frac{\pi \mathbf{I}_\lambda(\theta, \theta_0, \phi)}{\mu_0 \mathbf{F}_\lambda}, \qquad (1)$$

where θ and θ_0 are the viewing and illumination zenith angles, respectively, ϕ is the azimuthal angle between the viewing direction and the illumination direction so that forward and backward scattered photons represent azimuth angles of 0° and 180°, respectively, $\mu_0 = \cos \theta_0$, I_λ is the measured reflected radiance; and F_λ is the collimated irradiance. The collimated irradiance F_λ is computed by weighting the solar flux at the top of the atmosphere with the spectral response function of each band, taking into account the effects of the elliptical orbit of the Earth around the Sun.

[8] The BRDF is dimensionless and directly normalized to the reference illumination irradiance. This avoids the potential problems that the illumination source may not be covered entirely by the instrument instantaneous field of view (IFOV) and/or not be captured by the viewing geom-

Table 1. Current CAR Specifications

Platform	University of Washington CV-580 aircraft
Ground speed	80 m s^{-1} (nominal)
Total field of view	190°
IFOV	17.5 mrad (1°)
Imaging modes	4 (zenith, BRDF, starboard, and nadir)
Pixels per scan line	382
Scan rate	1.67 scan lines per second (100 rpm)
Spectral channels (μm; bandwidth (FWHM))	14 (8 continuously sampled and last 6 in filter wheel): 0.340 (0.009), 0.381 (0.006), 0.472 (0.021), 0.682 (0.022), 0.870 (0.022), 1.036 (0.022), 1.219 (0.022), 1.273 (0.023), 1.556 (0.032), 1.656 (0.045), 1.737 (0.040), 2.103 (0.044), 2.205 (0.042), 2.302 (0.043)
Output channels	9 channels at 16 bits
Data rate	61.85 MB hr^{-1}
Instrument mass	42 kg
Radiometric calibration	Laboratory integrating sphere measurements before and after research mission
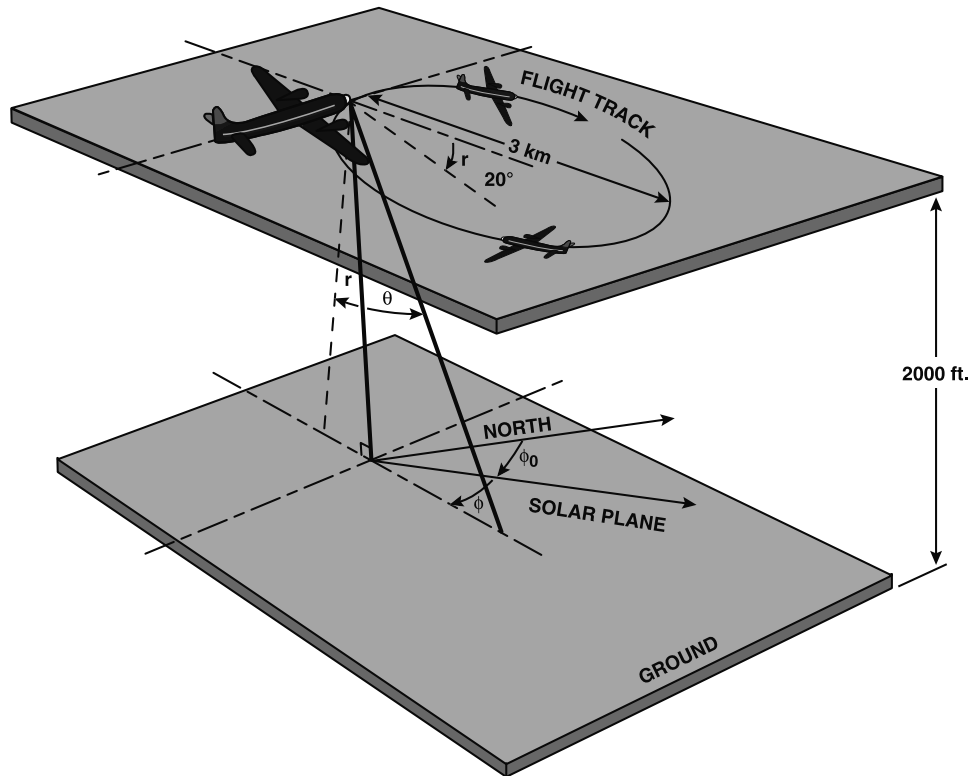
Figure 3. Schematic illustration of a clockwise circular flight track for measuring surface bidirectional reflectance from nadir to the horizon as well as much of the transmittance pattern from near zenith to the horizon. The plane banks at a roll angle r of about 20° as it circles a target of interest. Each orbit takes ~2.5 min to complete and consists of a circle of about 3 km in diameter. Adapted from the study of *King* [1992].

etry, as well as to prevent possible signal saturation due to instrument dynamic range [*Tsay et al.*, 1998]. However, it is important to remember that by definition, the BRDF is a derivative with instantaneous values that can never be measured directly because truly infinitesimal elements of a solid angle do not include measurable amounts of radiant flux [*Nicodemus et al.*, 1977]. Real measurements approximate the BRDF with nonzero values of intervals of solid

Table 2. Comparison of MODIS and CAR Surface Reflectance

Sensor	Date	Solar Zenith Angle (°)	View Zenith Angle (°)	Relative Azimuth Angle (°)	Reflectance at λ (μm)			
					0.470	0.670	0.870	1.250
			Skukuza (25.03°S, 31.51°E)					
MODIS	30 Aug.	47.79	63.07	54.16	0.0539	0.1305	0.2770	0.3933
CAR	29 Aug.	67.23	63.07	54.16	−0.0240	0.0710	0.1870	0.2560
MODIS	1 Sept.	34.98	62.47	253.36	0.0355	0.0575	0.1343	0.2067
CAR	1 Sept.	34.98	62.47	253.36	0.0010	0.1710	0.3610	0.4390
			Maun (20.00°S, 23.58°E)					
MODIS	28 Aug.	32.98	53.35	247.48	0.0512	0.1009	0.2126	0.3089
CAR	2 Sept.	27.94	53.35	247.48	−0.0440	0.1310	0.2690	0.4070
			Mongu (15.44°S, 23.26°E)					
MODIS	1 Sept.	31.66	1.85	234.47	0.0535	0.1058	0.2377	0.3365
CAR	6 Sept.	30.72	1.85	234.47	−0.0120	0.1470	0.2880	0.3740
MODIS	10 Sept.	29.60	12.45	49.61	0.0564	0.1091	0.2490	0.3602
CAR	10 Sept.	29.60	12.45	49.61	0.0020	0.1220	0.2670	0.3520
			Etosha Pan (18.98°S, 15.98°E)					
MODIS	15 Sept.	31.92	27.79	49.33	0.4940	0.5313	0.5926	0.4630
CAR	16 Sept.	32.72	27.79	49.33	0.2690	0.3940	0.3970	0.3970
			Sua Pan[a] (25.03°S, 31.51°E)					
MODIS	8 Sept.	30.24	42.92	244.14	0.2345	0.3345	0.3921	0.4373
CAR	3 Sept.	28.47	42.92	244.14	0.4040	0.6310	0.6240	0.6160

[a]For this site, comparisons have been made between MISR, PARABOLA, and CAR (W.A. Abdou, Jet Propulsion Laboratory, personal communication, 2002). The CAR and PARABOLA data are in very good agreement at all view angles and at all channels. MISR, like MODIS, is shown to underestimate the BRDF in the backscattering direction.
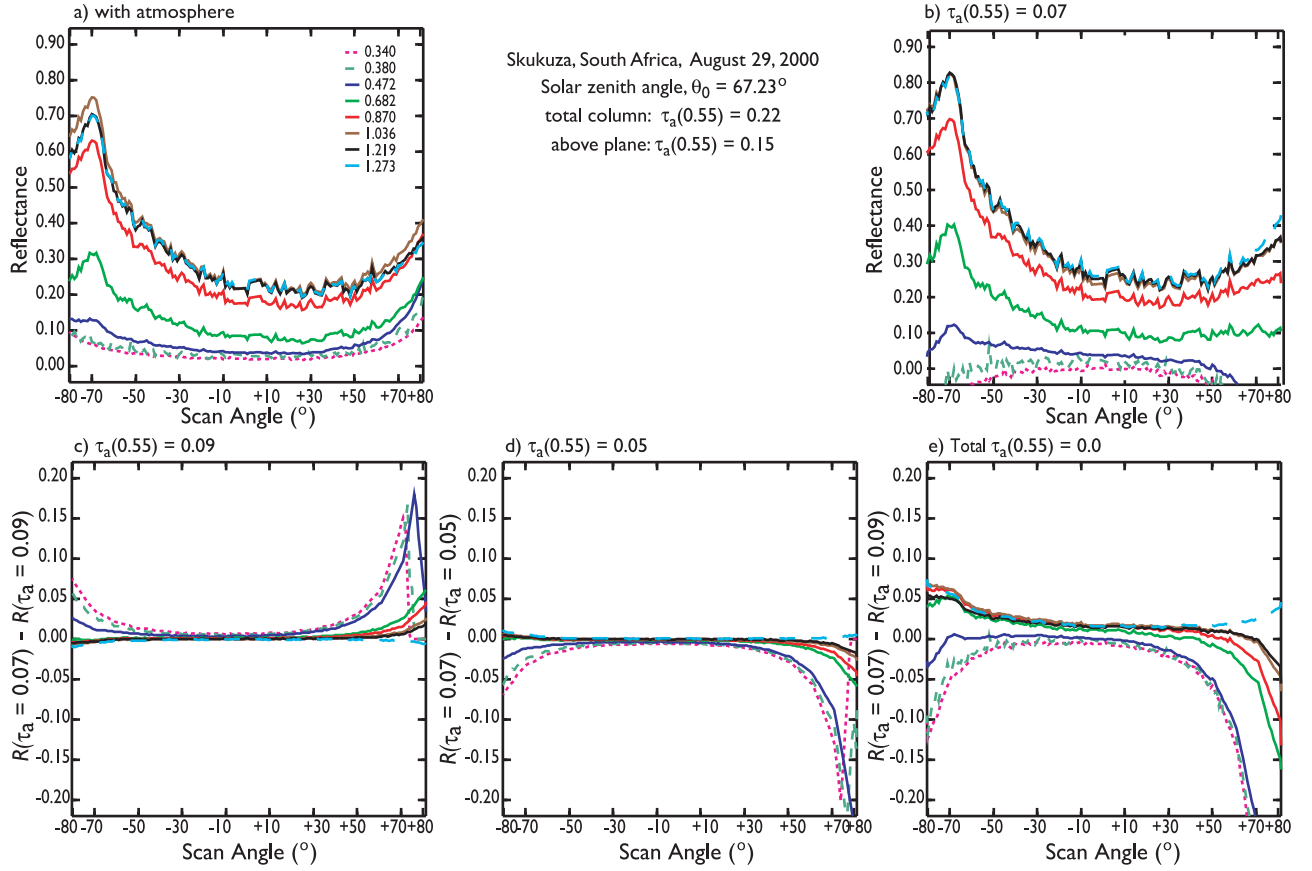
Figure 4. Angular distribution of bidirectional reflectance function in the principal plane (i.e., the vertical plane containing the Sun) for measurements taken over Skukuza, South Africa (25.0°S, 31.5°E) to demonstrate the uncertainty associated with atmospheric correction. (a) No atmospheric correction has been applied. (b) Atmospheric correction has been applied for $\theta_0 = 67.8°$, $\tau_a^{total}(0.550) = 0.22$, and $O_3 = 300$ m atm cm, where $\tau_a(0.550) = 0.07$ and $H_2O = 0.94$ g cm^{-2} below the plane. We have assumed a bimodal aerosol size distribution with complex index of refraction, $n(\lambda) = 1.51 - 0.021i$. (c) Difference in reflectance between atmospheric correction below the plane of $\tau_a(\lambda) = 0.07$ and $\tau_a(\lambda) = 0.09$. (d) Same as (c) but difference in reflectance between $\tau_a(\lambda) = 0.07$ and $\tau_a(\lambda) = 0.05$. (e) Same as (b) but difference in reflectance between $\tau_a(\lambda) = 0.07$ and $\tau_a(\lambda) = 0.0$ for the total column.

angles for source and view directions, and hence, yield only average values over the angular intervals. The definition of R_λ in (1) assumes a single direction for irradiance and reflectance over an area of a uniform and isotropic surface. This is the equation we have used to compute the BRDF discussed in this study.

[9] From the BRDF, we can derive the spectral albedo r_λ, the radiance reflected from the surface into all viewing directions and solid angles, by integrating the reflection function over solid angle. Hence, (1) becomes

$$\mathbf{r}_\lambda = \frac{1}{\pi} \int_0^{2\pi} \int_0^{\pi/2} \mathbf{R}_\lambda(\theta, \theta_0, \phi) \cos\theta \sin\theta d\phi,$$

$$\cong \frac{1}{\pi} \sum_{i=1}^{M} \sum_{j=1}^{N} \mathbf{I}_\lambda(\theta, \theta_0, \phi_j) \cos\theta_i \sin\theta_i \Delta\theta_i \Delta\phi_j, \qquad (2)$$

where (i,j) are indices for discretization of θ and ϕ over the hemisphere. In the present study we will not present albedo calculations, but will leave such comparisons with the

spectral albedo from the Solar Spectral Flux Radiometer (SSFR) onboard the Convair CV-580 [*King et al.*, 2003] and other related instrumentation during SAFARI 2000 to a future study.

3. Measurement Methods

3.1. Description of the Instrument

[10] In the past, we described the CAR [*King et al.*, 1986], but the instrument has recently undergone several upgrades that include (1) adding and/or substituting optical channels to suit specific experimental objectives and (2) replacing the data system with a new data system with onboard signal digitization at 16 bit dynamic range and with improved signal-to-noise characteristics (see www.car.gsfc. nasa.gov for further details). Since these upgrades have not been described previously, we provide a short overview of the instrument in its present configuration.

[11] The CAR (Figure 2) is an airborne multiwavelength scanning radiometer that can perform several functions including (1) determining the single scattering albedo of

Figure 5. Photographs of the BRDF sites at (a) Skukuza, South Africa taken from a 22 m tower, 24 March 2000, (b) Maun, Botswana taken from a 10 m tower, 3 March 2000, (c) Mongu, Zambia taken from a 33 m tower, 2 September 2000, (d) Etosha Pan, Namibia 13 September 2000, (e) Sua Pan, Botswana, 13 September 2000, and (f) marine stratus off the Namibian coast, 13 September 2000 ((a−c) were taken by Jeff Privette, NASA GSFC, while (d−f) were obtained by the RC-10 camera aboard the ER-2 flying ∼20 km above the surface).

clouds at selected wavelengths in the UV, visible, and near-infrared [*King*, 1981; *King et al.*, 1990], (2) measuring the angular distribution of scattered radiation of various surfaces types, and (3) acquiring imagery of clouds and the Earth's surface. The CAR was designed to operate from a position mounted on an aircraft, either the tail or the nose, so that its scan is unimpeded as it scans from zenith to nadir.

[12] The CAR is capable of measuring scattered light in fourteen spectral bands. The scan mirror, rotating at 100 rpm, directs the light into a Dall-Kirkham telescope where the beam is split into nine paths. Eight light beams pass through beam splitters, dichroics, and lenses to individual detectors (0.34−1.27 μm), and finally are registered by eight data channels. They are sampled simultaneously and continuously. The ninth beam passes through a filter wheel to a detector with a Stirling cycle cooler. Signals registered by the ninth data channel are selected from among six spectral channels (1.55−2.30 μm) on a filter wheel. The filter wheel can either cycle through all six spectral bands at a pre-

e) Sua Pan

f) Marine Stratus

Figure 5. (continued)

scribed interval (usually changing filter every fifth scan line), or lock onto any one of the six spectral bands and sample it continuously.

[13] The CAR scan mirror rotates 360° in a plane perpendicular to the direction of flight and the data are collected through a 190° aperture. In the normal mode of operation onboard the CV-580 aircraft, the CAR views 190° of the Earth−atmosphere scene around the starboard horizon. This configuration permits observations of both local zenith and nadir with as much as a 5° aircraft roll. In addition to the starboard viewing mode, the CAR instrument can now be rotated in-flight into three other viewing positions: (1) downward-looking imaging mode, (2) upward-looking imaging mode, and (3) a dedicated BRDF viewing mode. Table 1 summarizes the characteristics of the CAR sensor, platform, and scanning system as applicable during SAFARI 2000.

3.2. Calibration of the CAR

[14] Radiometric calibration and spectral response measurements were made at NASA Goddard Space Flight Center (GSFC) and at the NASA Ames Research Center (ARC) Airborne Sensor Facility, respectively. The GSFC 1.83 m (aperture diameter ∼0.25 m) integrating sphere was used for calibration of the CAR spectral channels in the visible and near-infrared region while the GSFC 0.51 m (aperture diameter ∼0.20 m) integrating sphere was used for calibration of the UV channels at 0.34 and 0.38 μm. The 1.83 m sphere is internally illuminated by a maximum of 16 quartz tungsten halogen lamps, GE type Q 6.6A/T4/5CL, with each lamp rated at 200 W. The 0.51 m UV sphere, on the other hand, is illuminated by a maximum of 4 lamps, each

rated at 150 W and the lamp current stabilized at 6.0 ± 0.5 mA (S. Janz, GSFC, personal communication, 2002). The insides of both spheres are coated with a highly diffuse and reflective $BaSO_4$ paint. Calibration of the 1.83 m sphere is traceable to the National Institute of Standards and Technology (NIST) using a Czerny-Turner type monochromator to transfer an irradiance calibration from a 1 kW FEL type working standard lamp (J. Cooper, GSFC, personal communication, 2002). The 0.51 m UV sphere calibration transfer is performed using an Ebert-Fastie double monochromator against several NIST 1 kW lamps.

[15] During calibration, the CAR instrument is placed roughly 25 cm from the entrance aperture to get uniform light intensity across the field of view. The instrument is then illuminated at different light levels to determine radiometric response across the dynamic range of the detector. Conversion of the digital counts or digital numbers (DNs) from the instrument to radiance is determined from instrument response for at least two known radiance levels and then determining the instrument gain (slope) and offset (intercept) for each wavelength across the sensor band pass. The estimated errors associated with radiometric conversion vary from ±1% to ±3% for all spectral channels.

[16] Radiometric calibration was performed prior to and after the dry season SAFARI 2000 field experiment. In order to determine a suitable calibration for a given flight during the experiment, we assumed a linear change between the preflight and postflight calibration and as a function of only the number of flights flown during SAFARI 2000. In this case, there were a total of 25 flights flown, 2 during the instrument flight test, and 23 during the field experiment. We
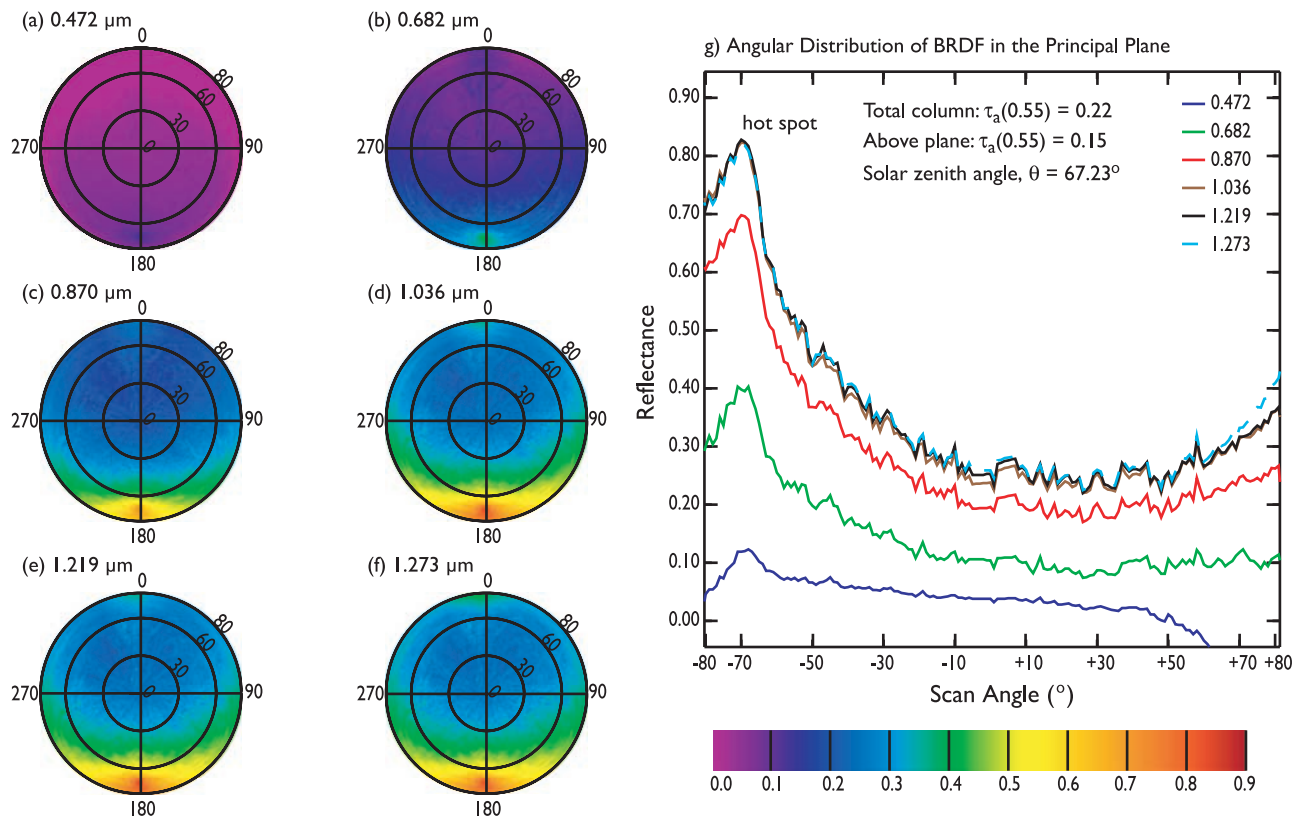
Figure 6. Spectral BRDF for selected CAR channels obtained over Skukuza, South Africa (25.0°S, 31.5°E) in late winter conditions (29 August 2000). In all polar plots, the viewing zenith angle is represented as the radial distance from the center and the azimuth as the length of arc on the respective zenith circle. The principal plane resides in the 0°–180° azimuthal plane with the Sun located in the 180° azimuthal direction and is shown to the right of the polar plots. With this definition, the upper half circle represents forward scattering and the lower half circle backscattering. Atmospheric correction was applied using the following inputs: solar zenith angle $\theta_0 = 67.23°$, total column $\tau_a(\lambda) = 0.22$ ($\tau_a(\lambda) = 0.15$ above the plane, $\lambda = 0.550 \, \mu m$), and total column $H_2O = 1.64 \, g \, cm^{-2}$ ($H_2O = 0.73 \, g \, cm^{-2}$ above the plane). Other input parameters required for performing correction are as specified in Figure 4b.

note that the calibration ratios, postflight/preflight, vary between 1.048 (at $\lambda = 0.340 \, \mu m$) and 1.292 (at $\lambda = 1.556 \, \mu m$).

[17] For the spectral calibration, all spectral bands were scanned with a monochromator illuminated with a tungsten–halogen lamp. The monochromator output was collimated and expanded to full input pupil of the CAR, and the beam was chopped to allow use of phase-sensitive signal detection. From these measurements, we determined the instrument system spectral response, central wavelengths, and corresponding spectral band pass characteristics at each of the 14 spectral channels.

3.3. Measurements of BRDF

[18] To measure the BRDF of the surface–atmosphere system, the aircraft flew at a roll angle of ~20° flying in a circle about 3 km in diameter above the surface, taking roughly 2–3 min to complete an orbit (see Figure 3). The SAFARI 2000 measurements were generally obtained at an altitude of ~600 m above the targeted surface and under clear sky conditions. Therefore, at a 1° IFOV the pixel resolution is about 10 m at nadir and about 270 m at an 80° viewing angle from the CAR. Multiple circular orbits were acquired over a selected surface so that average BRDFs

average out small-scale surface and atmospheric inhomogeneities. With this configuration, the CAR collects between 76,400 and 114,600 directional measurements of radiance per channel per complete orbit.

[19] We believe using the CAR in this manner is the most mobile and efficient way of measuring a complete surface BRDF, but it is still necessary to correct for atmospheric scattering effects both above and below the aircraft in order to isolate the reflectance properties of the underlying surface in the absence of an atmosphere.

3.4. Atmospheric Correction

[20] We removed the effects of atmospheric absorption and scattering from our bidirectional reflectance functions using a new version of the second simulation of satellite signal in the solar spectrum (6S) model [*Vermote et al.*, 1997]. The 6S code is a radiative transfer model based on the successive orders of scattering method. The spectral resolution of the model is 2.5 nm, and the aerosol layer is divided into 13 layers with a scale height of 2 km. The model assumes the atmosphere consists of fixed gases: O_2, O_3, H_2O, CO_2, CH_4, and N_2O. The concentration of O_2, CO_2, CH_4, and N_2O are assumed to be constant and
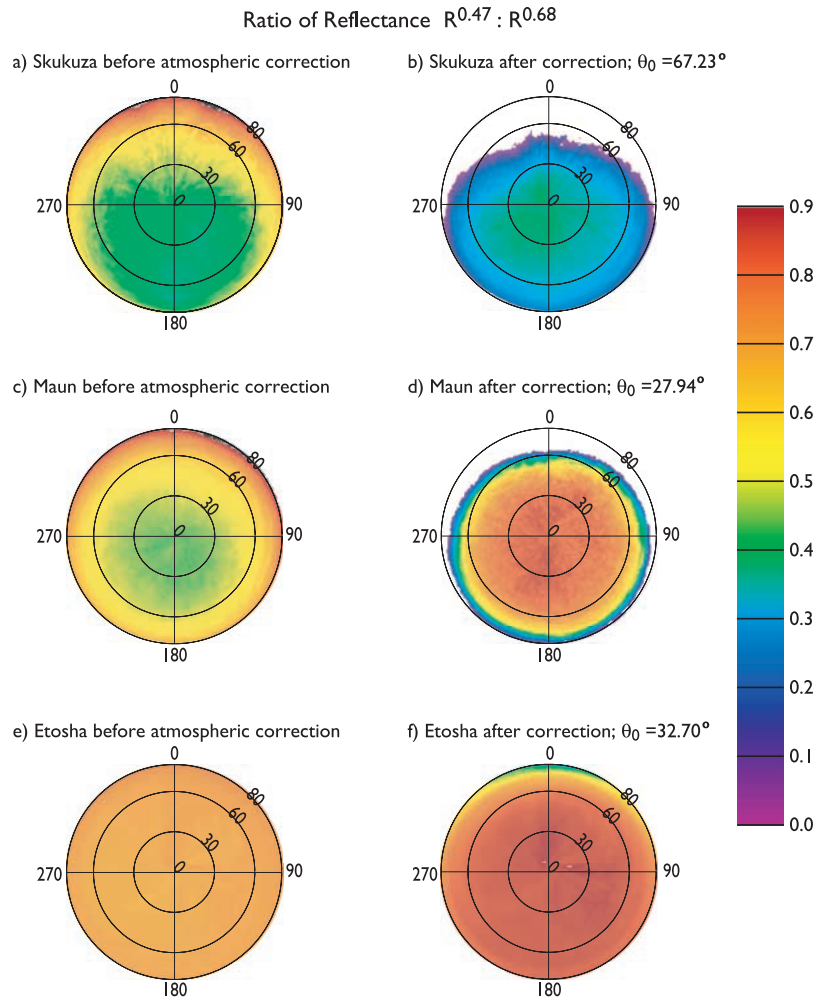
Figure 7. Angular variation of ratio of $R^{0.472}$ versus $R^{0.682}$ for different surfaces before and after correction of atmospheric scattering and absorption.

uniformly mixed in the atmosphere [*Vermote et al.*, 1997]. The 6S model allows us to determine the attenuation of solar irradiance under cloudless conditions at the surface. It removes the effects of Rayleigh scattering, aerosol attenuation, and ozone and water vapor absorption, provided we know the key characteristics of the atmosphere, such as the atmospheric optical thickness, aerosol model, and absorbing gas concentration. The CAR measurements for the SAFARI 2000 intensive field campaign were coincident and colocated with others, both ground based and airborne, needed as input to the 6S model. For example, the Ames Airborne Tracking Sun photometer [*Schmid et al.*, 2003] was also flown aboard the University of Washington CV-580 aircraft, providing measurements of aerosol optical depth and water vapor at 14 discrete channels in the UV, visible, and near-infrared regions of the electromagnetic spectrum at the same locations and time as the CAR BRDF measurements were obtained. Similarly, ground-based Sun photometer measurements were obtained during the time and location of most CAR BRDF observations. Thus, where possible, we have used the corresponding observations of aerosol optical depth (τ_a) and water vapor and assumed a bimodal size distribution of aerosol with parameters obtained from the study of *Dubovik et al.* [2002].

[21] We have also checked how the atmospheric correction is biased by errors in aerosol optical thickness. Of course there could be other sources of uncertainty, such as calibration errors, experimental errors, and failure of the radiative transfer model [cf. *Salomonson and Marlatt*, 1971; *Dubovik and King*, 2000], but they are outside the scope of this study. Figure 4a shows reflection function measurements in the principal plane of the Sun as obtained over Skukuza, South Africa before atmospheric correction is applied. Figure 4b shows results obtained after correcting for atmospheric absorption and scattering using the 6S radiative transfer code. The 6S computation was performed assuming a homogenous surface with a Lambertian reflectance, a solar zenith angle $\theta_0 = 67.23°$, and an aerosol optical thickness $\tau_a(0.550 \ \mu m) = 0.22$ (0.15 above the aircraft that was flying at $\sim$600 m above the surface). The total column water vapor q = 1.67 g cm^{-2} (0.73 g cm^{-2} above the aircraft) is obtained from ground-based and airborne Sun photometer measurements. The O_3 column amount was assumed to be 300 m atm cm. We further assumed a bimodal aerosol size distribution with a complex refractive index n(λ) = 1.51 − 0.021i, in accordance with the study of *Dubovik et al.* [2002].
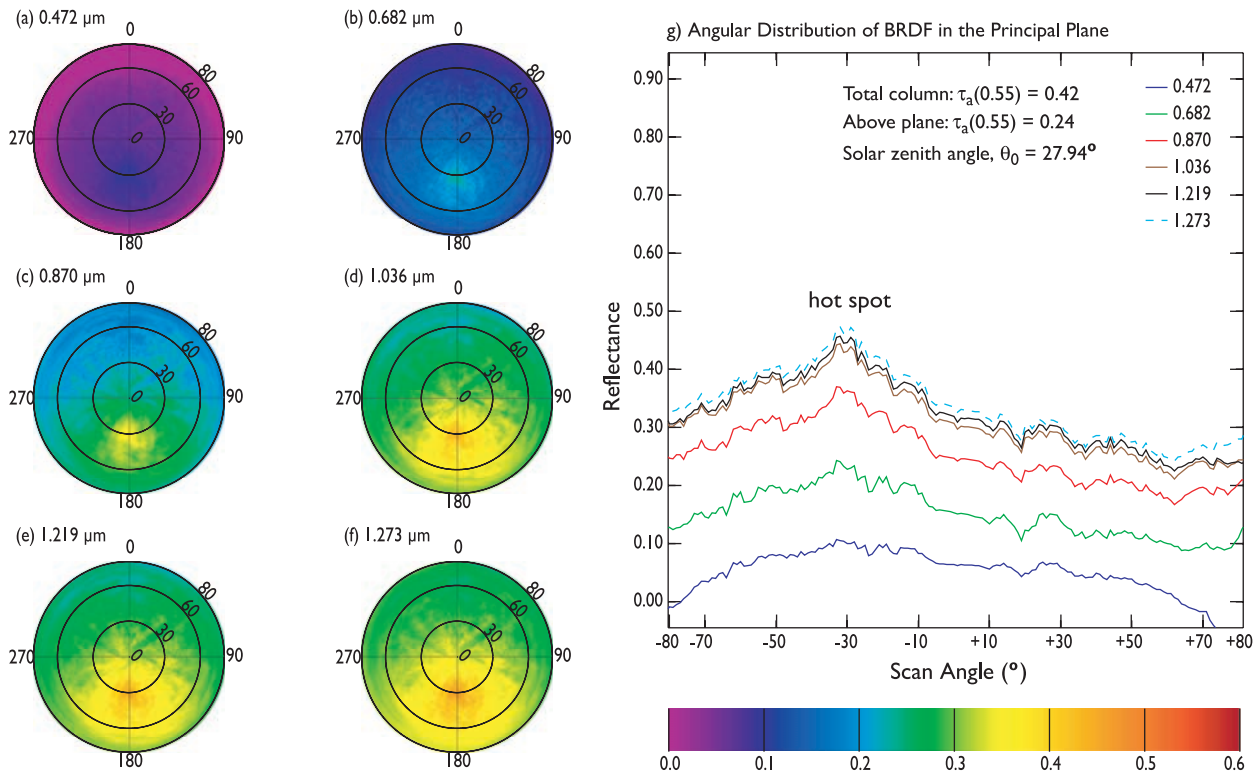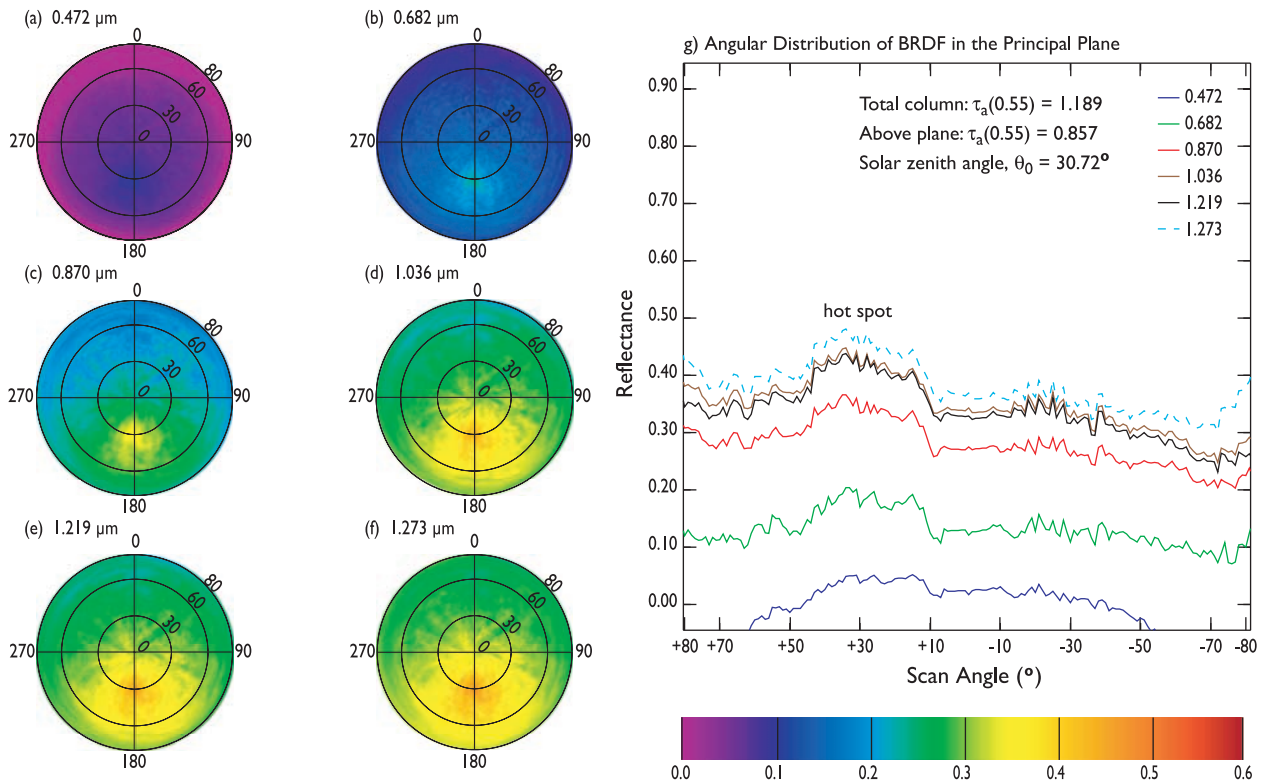
Figure 8. Spectral BRDF for selected CAR channels obtained over Maun, Botswana (20.0°S, 23.6°E) in late winter conditions (2 September 2000). Atmospheric correction was applied using the following inputs: solar zenith angle $\theta_0 = 27.94°$, total column $\tau_a(\lambda) = 0.42$ ($\tau_a(\lambda) = 0.22$ above the plane, $\lambda = 0.550$ μm), and total column $H_2O = 1.13$ g cm^{-2} ($H_2O = 0.39$ g cm^{-2} above the plane). Other input parameters required for performing correction are as specified in Figure 4b.

[22] Comparing Figures 4a and 4b, we note an enhanced reflectance after correction in the backscattering direction and a decrease in reflectance, especially at $\lambda = 0.472$ μm, in the forward scattering direction, especially for view angles $\theta > 30°$. The fact that this affects the blue channel more suggests a greater uncertainty in assumed and/or measured aerosol optical properties in this wavelength region. By assuming an error of ±0.02 in aerosol optical thickness below the aircraft [cf. *Dubovik et al.*, 2000], we recomputed the atmospheric correction with the other conditions remaining the same and then subtracting the resulting reflectance from the reflectance obtained for the observed τ_a. The resultant differences, plotted as a function of view zenith angle, are shown in Figures 4c and 4d. Although there is little effect in the backward scattering direction, the effect is significant in the forward scattering direction, especially at $\lambda \leq 0.472$ μm. This is further shown by assuming a total $\tau_a = 0.0$ (Figure 4e). Clearly, errors in $\tau_a \geq 0.02$ lead to an overestimation (underestimation) of path radiance in the forward scattering direction, especially at the shorter wavelengths under low Sun angles, resulting in an overcorrection (undercorrection) of the measured reflectance.

[23] To ensure that we have a meaningful and consistent atmospheric correction, we decided to do a simple intercomparison between atmospherically corrected surface reflectance obtained with the CAR- and MODIS-derived surface reflectance obtained over the same targets and for similar geometric conditions (Table 2). However, for Sku-

kuza, where the BRDF measurements were acquired at a very low Sun angle $\theta_0 = 67.23°$, we interchanged the view zenith and solar zenith angles in accordance with the Helmholtz principle of reciprocity [*Chandrasekhar*, 1960] in order that we could have a close match with MODIS geometry. Apparently, this does not appear to help since there is poor agreement between CAR measured surface reflectance and MODIS surface reflectance. Good agreement is noted for Maun and Mongu for $\lambda > 0.472$ μm. For example, over Maun at $\lambda = 0.670$ μm, MODIS reports a reflectance ~10% whereas CAR observes 13%. This is a reasonable agreement considering that the Sun angles were slightly different, ~33° during the MODIS overpass and ~28° during CAR BRDF measurements. Over Mongu, where the conditions are similar, there is a very close correspondence, especially in the forward scattering direction ($\theta = 12.45°$, $\phi = 49.61°$) where the reflectance ~11% for MODIS and ~12% for CAR at $\lambda = 0.670$ μm. Over Etosha and Sua Pans, which are bright surfaces that reflect strongly in the backscattering direction (see the following section), there is not such good agreement. It appears that the MODIS reflectance values have not been corrected for directional effects and that is probably why they are exaggerated in the different viewing planes. This observation is strengthened by the good agreement between CAR and PARABOLA (Portable Apparatus for Rapid Acquisition of Bidirectional Observations of Land and Atmosphere)

Figure 9. Spectral BRDF for selected CAR channels obtained over Mongu, Zambia (15.4°S, 23.3°E) in late winter conditions (6 September 2000). Atmospheric correction was applied using the following inputs: solar zenith angle $\theta_0 = 30.72°$, total column $\tau_a(\lambda) = 1.19$ ($\tau_a(\lambda) = 0.86$ above the plane, $\lambda = 0.550$ μm), and total column $H_2O = 1.79$ g cm^{-2} ($H_2O = 0.84$ g cm^{-2} above the plane). Other input parameters required for performing correction are as specified in Figure 4b.

measurements over Sua Pan (W. A. Abdou, Jet Propulsion Laboratory, personal communication, 2002).

[24] We should point out here that 6S is normally used in performing atmospheric correction for data acquired at view angles from nadir to around 75° off-nadir [*Vermote et al.*, 1997]. We decided to extend it to 89° off-nadir to test its performance on our data. The model is not able to reproduce gross features at slant viewing directions and therefore we have decided to exclude from our plots all data for view angles greater than 80°.

4. Results From Observations

[25] In this section, we will discuss BRDF measurements over savanna (Skukuza, Maun, and Mongu), salt pans (Sua and Etosha), and marine stratus clouds. These surfaces have different bidirectional reflectance distribution functions and will therefore be treated separately. All BRDFs are corrected for atmospheric scattering and absorption and the parameters used in performing the correction are indicated in the figure legends.

4.1. The BRDF of the African Savanna

[26] Most CAR BRDF measurements were obtained over sites located in the savanna biome of southern Africa, including Skukuza, South Africa (25.0°S, 31.5°E), Maun, Botswana (20.0°S, 23.6°E) and Mongu, Zambia (15.4°S, 23.3°E). These three locations are core sites for validation of

land and atmospheric operational products from the Earth Observing System (EOS) Terra satellite using above-canopy towers for semiautomatic and near-continuous measurement of canopy level radiation properties [*Morisette et al.*, 1999]. Although the three sites are located in different locations, they exhibit similar characteristics typical of a savanna ecosystem: a more-or-less continuous herbaceous cover and a discontinuous cover of trees or shrubs in varying proportions. However, a careful examination of photographs of the three sites (see Figures 5a–5c) reveals some conspicuous differences in the composition, structure, and density of the plant communities. These variations are attributable to the influence of moisture in an area, as well as differences in altitude, slope of the terrain, soil type, and the prevalence of fires [*Scholes and Archer*, 1997]. Soil seems to be one of the major factors influencing different species in the three sites. We examine the reflectance characteristics from these three sites, starting with Skukuza.

4.1.1. Skukuza, South Africa

[27] Skukuza is the hottest and most arid region in the Kruger National Park. The vegetation at Skukuza is dominated by knob thorn trees (*Acacia nigrescens*) with their relatively narrow crown and sparse canopy, and leadwood (*Combretum imberbe*), a very tall, high branched, majestic tree with sparse foliage (see Figure 5a). These trees grow to heights of 18–20 m in this region of granite soil.
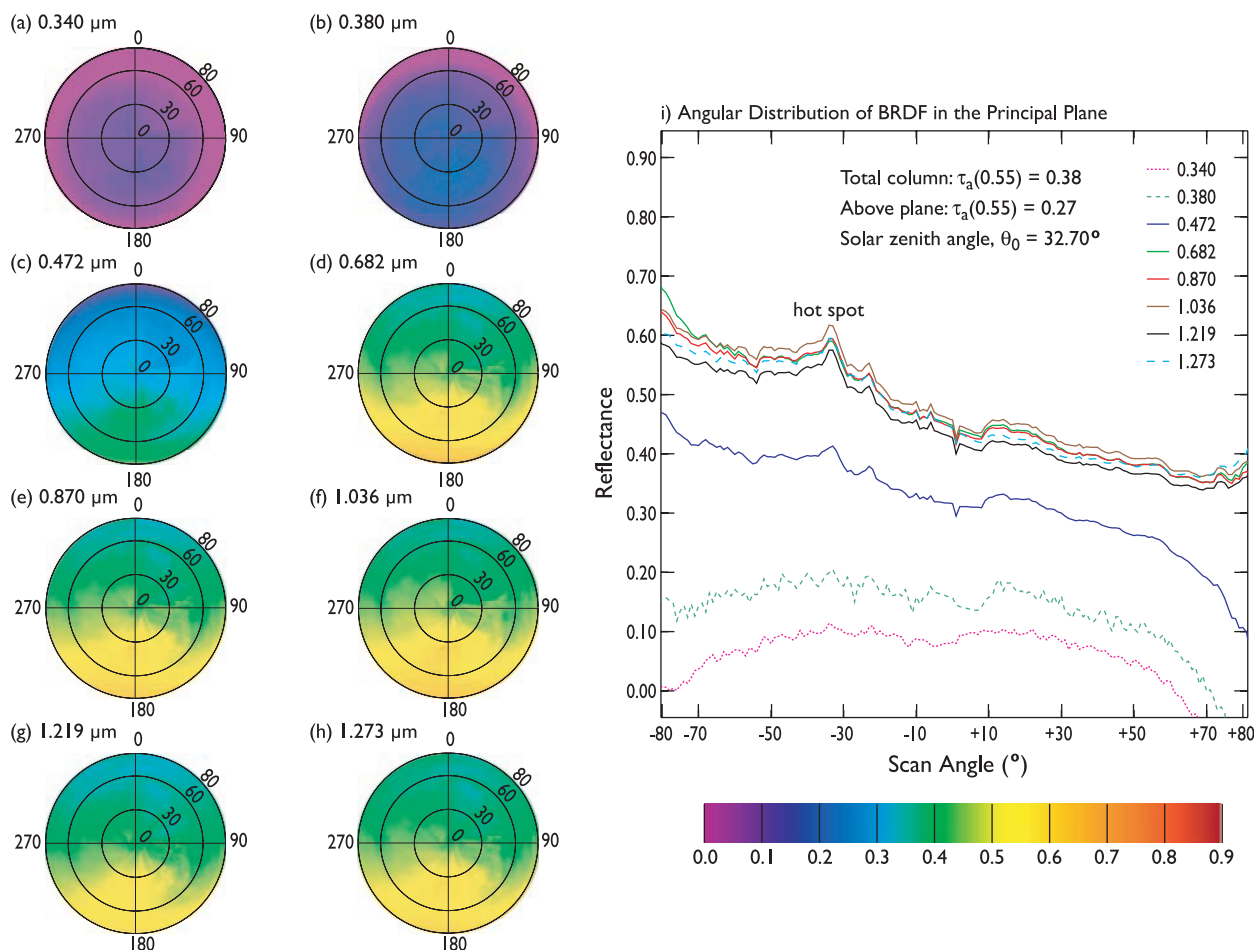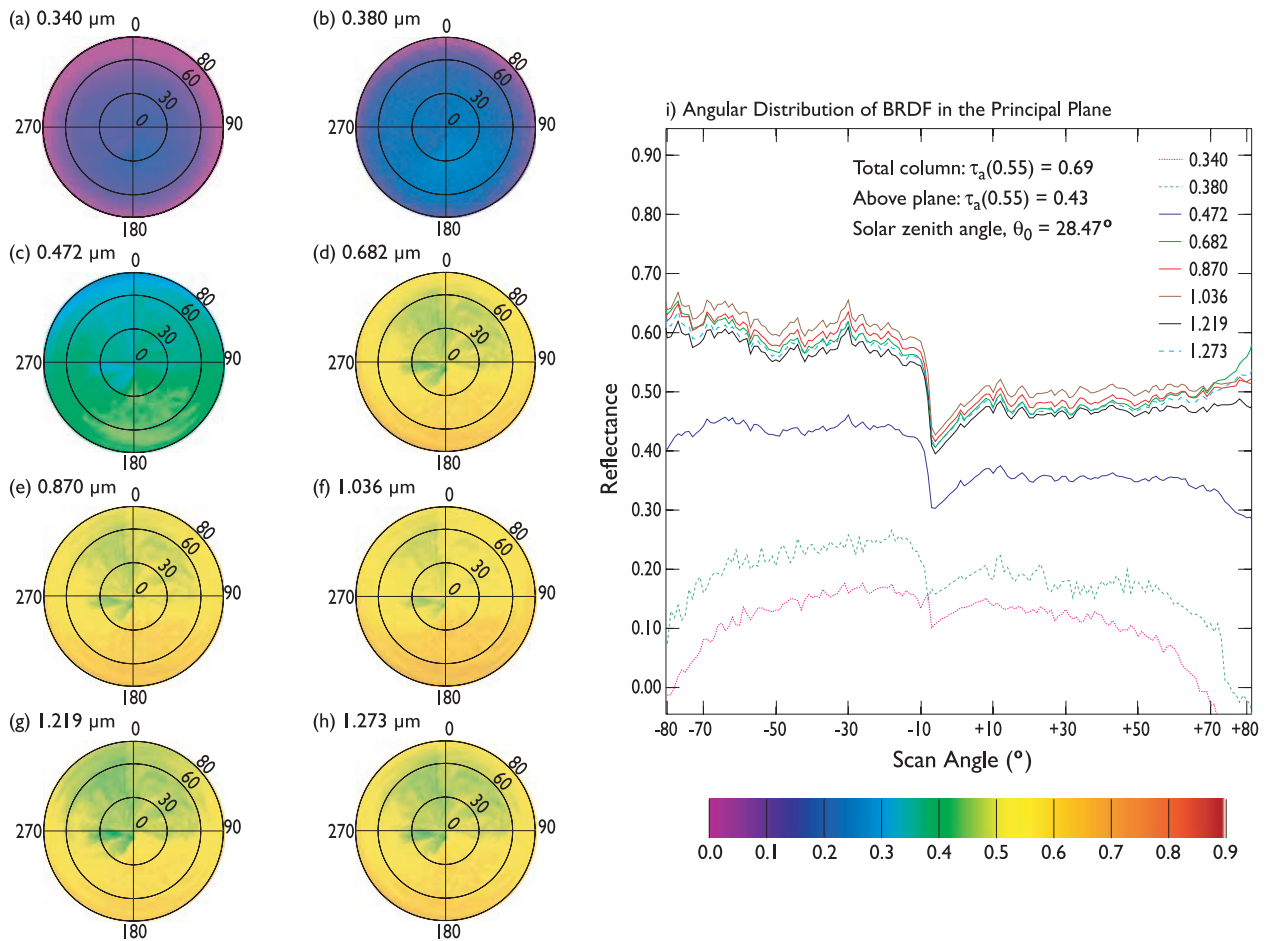
Figure 10. Spectral BRDF for selected CAR channels obtained over Etosha Pan (19.0°S, 16.0°E) in late winter conditions (16 September 2000). Atmospheric correction was applied using the following inputs: solar zenith angle $\theta_0 = 32.72°$, total column $\tau_a(\lambda) = 0.38$ ($\tau_a(\lambda) = 0.27$ above the plane, $\lambda = 0.550$ μm), and total column $H_2O = 1.13$ g cm^{-2} ($H_2O = 0.84$ g cm^{-2} above the plane). Other input parameters required for performing correction are as specified in Figure 4b.

[28] Figure 6 shows the BRDF of the surface at Skukuza (25.0°S, 31.5°E) and a transect of reflectance through the principal plane (the vertical plane containing the Sun, where $\phi = 0°$ and $\phi = 180°$), for six discrete wavelengths between 0.472 and 1.273 μm. These measurements were obtained from 1338 to 1406 UTC for solar zenith angle $64° < \theta_0 < 70°$. The reflection function shows a steep increase in magnitude in the backscattering direction ($\phi = 180°$), is low at nadir ($0.05 < R_\lambda \leq 0.30$; $0.472 \leq \lambda \leq 1.273$ μm), and reaches a maximum ($0.10 < R_\lambda < 0.80$; $0.472 \leq \lambda \leq 1.273$ μm) in the antisolar direction, $\theta = 70°$, and then decreases thereafter. The backscattering peak is a common feature observed in vegetation canopies when the Sun and the observer are at the same position in the hemisphere [*Li and Strahler*, 1992]. It occurs because the leaves, stems and trunks that comprise the plant hide their own shadows under these conditions, and thus the scene appears bright due to maximal single scattering [*Wanner et al.*, 1997]. The reflection function is nearly invariable in the forward scattering plane, $\phi = 0°$, and varies between 0.05 and 0.3 for all spectral channels from nadir to $\theta = 50°$; after this view zenith angle the atmospheric correction seems to fail,

especially at $\lambda = 0.472$ μm, perhaps more due to dominance of multiple scattering in the forward scattering leading to longer optical path length that is very sensitive to even small errors in τ_a. The bowled shape of the BRDF across the principal plane is reminiscent of sparse trees and shrubs over dense grass (similar to the cerrado [*Tsay et al.*, 1998]) than to the more domed BRDFs of sparse trees and shrubs over bright soil as detected by NASA's Airborne Solid-State Imaging Spectrometer (ASAS) instrument during the Hydrology-Atmosphere Pilot Experiment in the Sahel (HAPEX SAHEL) [*Lewis et al.*, 1999]. A relationship between the angular reflectance function at all spectral channels ($R_{0.47} < R_{0.68} < R_{0.87} < R_{1.22} < R_{1.27} < R_{1.03}$) is noted to be generally true for all zenith angles. This means that simple parametric relations could be easily established for representing BRDF for this type of ecosystem. The higher values for the near-infrared are to be expected since vegetation absorbs more energy in the visible part of the solar spectrum than in the near-infrared [*Chen et al.*, 2000]. This characteristic of vegetation is used in remote sensing to monitor temporal evolution of greenness in vegetation [*Tucker*, 1979]. Similarly, relationship such as $R_{0.47} =$

Figure 11. Spectral BRDF for selected CAR channels obtained over Sua Pan, Botswana (20.6°S, 25.9°E) in late winter conditions (3 September 2000). Atmospheric correction was applied using the following inputs: solar zenith angle $\theta_0 = 28.47°$, total column $\tau_a(\lambda) = 0.69$ ($\tau_a(\lambda) = 0.43$ above the plane, $\lambda = 0.550$ μm), and total column $H_2O = 1.04$ g cm^{-2} ($H_2O = 0.46$ g cm^{-2} above the plane). Other input parameters required for performing correction are as specified in Figure 4b.

$0.5R_{0.67}$ used in remote sensing of aerosol optical thickness over land [*Kaufman et al.*, 1997; *King et al.*, 1999; *Gatebe et al.*, 2001] can also be verified as a function of view zenith and azimuthal angles (see Figure 7). Note that we blanked out values of reflectance ratio falling outside the range 0.0–0.9.

4.1.2. Maun, Botswana

[29] Maun is located east of the Okavango Delta and has vegetation dominated by medium-sized multistemmed mopane trees (*Colophospermum mopane*) (see Figure 5b) that grow to a height of 18 m in this region, with thickset stems and long, bare branches. The tree protects itself from excessive heat by folding its leaves along the midrib to preserve moisture, allowing rays of the Sun to pass directly to the ground, thereby casting a poor shadow on the ground. The BRDF and the principal plane reflectance at six discrete wavelengths between 0.472 and 1.273 μm are shown in Figure 8. The measurements over Maun tower (20.0°S, 23.6°E) were obtained on 2 September 2000 from 1029 to 1045 UTC when $27° < \theta_0 < 29°$. The reflection function, unlike that from Skukuza, shows a gradual increase in magnitude in the backscattering plane, $\phi = 180°$, is low at nadir ($0.05 < R_\lambda \leq 0.30$; $0.472 \leq \lambda \leq 1.273$ μm), and is a

maximum ($0.10 < R_\lambda < 0.50$; $0.472 \leq \lambda \leq 1.273$ μm) in the antisolar direction, $\theta = \theta_0 = 29°$. Because of the smaller solar zenith angle than that at Skukuza, and hence less shadow, the peak is not as pronounced and strong as it is for Skukuza. The reflection function is nearly invariable in the forward scattering plane, $\phi = 0°$, and varies between 0.05 and 0.3 for view zenith angles from nadir to $\theta = 80°$ for all spectral channels except 0.472 μm, where values seem unrealistic beyond $\theta = 50°$ due to effects of aerosol uncertainty in the atmospheric correction.

4.1.3. Mongu, Zambia

[30] Mongu is located in the western province of Zambia and is adjacent to the massive Zambezi River floodplain in an area of vegetation dominated by Miombo-related species 16–18 m in height (Figure 5c). Figure 9 shows the BRDF pattern at six discrete wavelengths between 0.472 and 1.273 μm and the corresponding principal plane reflectance of the surface near the Mongu tower (15.4°S, 23.3°E). The measurements were obtained on 6 September 2000 from 0847 to 0908 UTC when $28° < \theta_0 < 33°$. Notable in this figure is the lack of a clearly defined backscattering peak and a weak contrast between the backscattering and forward scattering directions. However, the BRDF pattern and reflectance
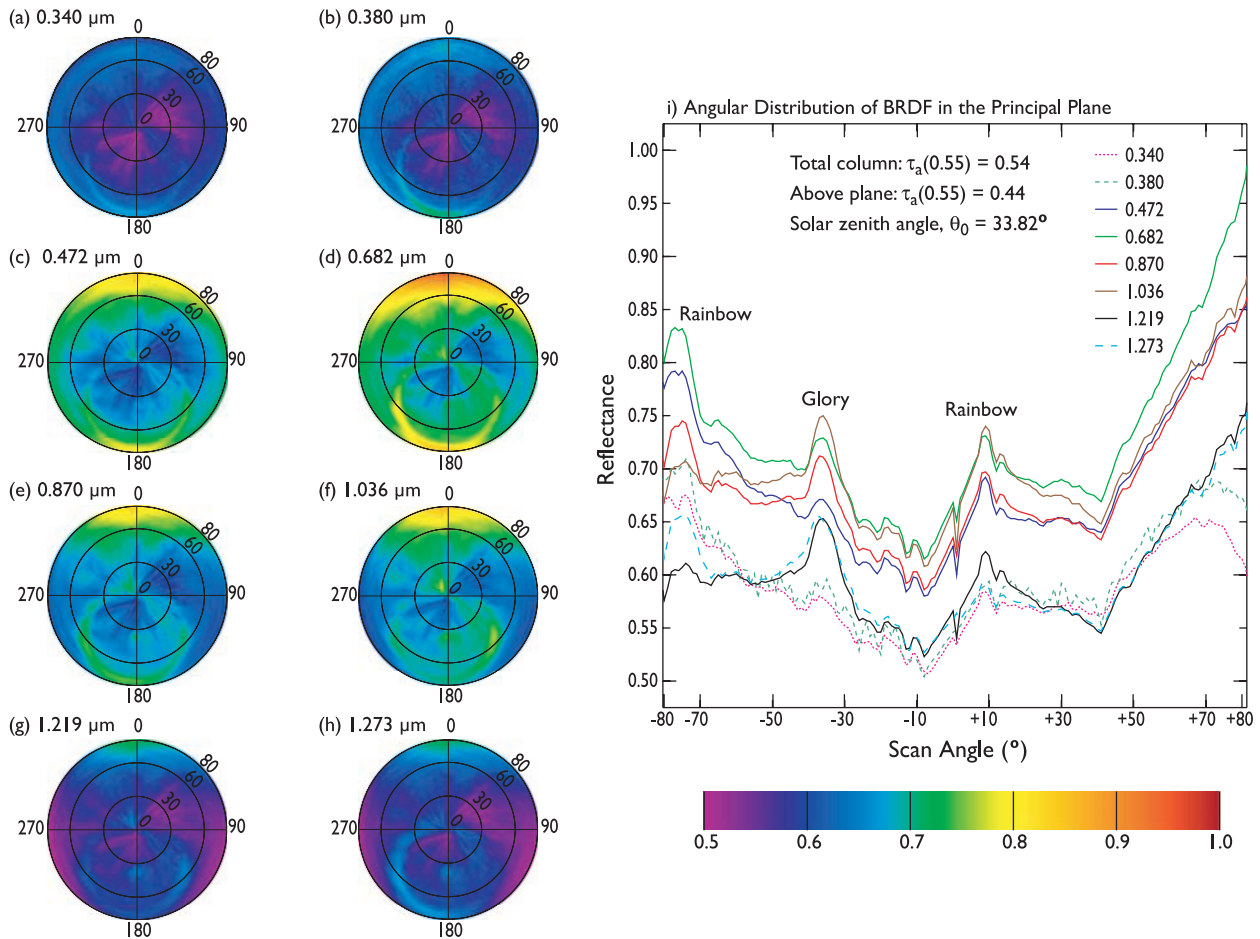
Figure 12. Spectral BRDF for selected CAR channels obtained over marine stratocumulus off the Skeleton coastline in Namibia (20.5°S, 13.1°E) in late winter conditions (13 September 2000). Atmospheric correction was applied using the following inputs: solar zenith angle $\theta_0 = 33.82°$, total column $\tau_a(\lambda) = 0.54$ ($\tau_a(\lambda) = 0.44$ above the plane, $\lambda = 0.550$ μm), and total column $H_2O = 0.86$ g cm^{-2} ($H_2O = 0.84$ g cm^{-2} above the plane). Other input parameters required for performing correction are as specified in Figure 4b.

magnitude in the principal plane look similar to those reported for Maun except for $\lambda = 0.472$ μm. The high aerosol optical thickness $\tau_a(0.472) = 1.10$ above the aircraft measured during these BRDF measurements over Mongu appears to affect the correction at the short wavelengths.

4.2. Salt Pans

[31] Because of their unique optical characteristics, we obtained BRDF measurements over two salt pans: Etosha Pan and Sua Pan. The Etosha Pan spans 5000 km^2 of desert-like landscape and is situated in northern Namibia, while Sua Pan covers roughly 3500 km^2 and is part of the Makgadikgadi Pans in northeastern Botswana. These salt pans are bare featureless surfaces, white in color from the dried salt, and unvegetated with little or no plant cover (see Figures 5d and 5e). Their surroundings are dominated by mopane and acacia scrubland and grasslands.

[32] Figure 10 shows the BRDF of Etosha Pan (19.0°S, 16.0°E) and a transect through the principal plane for eight discrete wavelengths between 0.34 and 1.27 μm. These measurements were obtained from 0904 to 0917 UTC for solar zenith angles $31° < \theta_0 < 33°$. For all spectral channels,

the reflection function is enhanced in the backward scattering direction, relative to the forward direction. The reflectance ranges from 0.6 at $\theta = 80°$ in the backscattering direction (antisolar direction) to 0.2 in the forward scattering direction at $\theta = 70°$ for $0.472 \leq \lambda \leq 1.273$ μm. Notable also is a small peak in the backscattering direction that occurs in opposition to the Sun at $\theta = 31°$. This appears to be a feature of bare soil rather than of a pure salt pan. Bare soil backscatters sunlight, resulting in a strong "hot spot" where radiance has been scattered back into the direction of the Sun [*Nolin and Liang*, 2000]. While a smooth surface of mineral particles would be forward scattering, soil aggregates create sufficient small-scale surface roughness that results in a dominant backscatter-ing effect in the soil BRDF pattern. Soil spectral reflectance is controlled by other factors as well, including soil particle size, texture, organic matter, clay, iron content, soil moisture, and surface roughness. These properties determine not only the magnitude of the spectral reflectance but also the position and depth of spectral absorption features. Soil reflectance tends to increase steadily from about 0.2 in the visible and rarely exceeds 0.5 in the near infrared [*Nolin and Liang*, 2000]. Since the measured reflectance of the pan is in the range 0.2–

0.6, we think that the salt pans are dominated by highly reflecting soil aggregates with very little organic matter.

[33] Figure 11 shows the BRDF of the Sua Pan (20.6°S, 25.9°E) and a transect through the principal plane for eight discrete wavelengths between 0.34 and 1.27 μm. The measurements reported here were obtained from 0949 to 1000 UTC for solar zenith angle $\theta_0 = 28.47°$. The BRDF pattern of Sua Pan is very similar to Etosha's enhanced reflectance in the backward scattering direction. The feature between $-10°$ and $+10°$ in the principal plane is a result of surface inhomogeneity that we were unable to avoid during our measurements.

4.3. BRDF of Marine Stratocumulus Offshore of Namibia

[34] The marine stratocumulus clouds off the western coast of southern Africa are layered clouds, associated with subtropical anticyclonic subsidence and cold water upwelling along the Benguela current [*Platnick et al.*, 2000]. These clouds are characterized by a well-defined cloud top height corresponding to a strong boundary layer inversion (Figure 5f). These clouds are impacted by both natural (sulfur from phytoplankton DMS production and decay processes) and anthropogenic sources (industrial and fire emission products) that can influence the clouds microphysical and optical properties, an effect that is not quantitatively well understood.

[35] Figure 12 shows the BRDF of marine stratus clouds and a transect through the principal plane of these clouds for eight discrete wavelengths between 0.34 and 1.27 μm. These measurements were obtained off the Namibian coast (20.5°S, 13.1°E) between 1228 and 1252 UTC for solar zenith angles $31° < \theta_0 < 36°$. Note the expanded scale of the color bar and reflectance axis, enabling more features and structure to be discerned. Visible in these BRDF observations for all spectral channels are pronounced circular brightness features, the rainbow and glory. These single scattering features are more distinct at 0.682 and 0.870 μm, and only barely visible at 0.340 μm, perhaps due more to lack of contrast perception. Looking at the angular distribution of BRDF in the principal plane (Figure 12i), we note that the primary rainbow has a peak at approximately $-75°$ and $+10°$, corresponding to ∼42° from the antisolar direction characterized by the glory feature. The magnitude of reflectance in all spectral channels is between 0.5 and 0.9.

[36] Observations of the glory in both visible and near-infrared wavelengths have good potential as an approach to measuring cloud top droplet size through remote sensing. *Spinhirne and Nakajima* [1994] show a direct dependence of the glory-scattering angle on effective particle radius near the cloud top. The important and relevant characteristic is that the measurements would be unquestionably accurate and unambiguous. Our data along with coincident cloud microphysics and other measurements from SAFARI 2000 experiment (see Appendix A by P. V. Hobbs in the work of *Sinha et al.* [2003]) [*King et al.*, 2003] should enable us to conceive interesting analyses and applications for radiation and remote sensing problems.

5. Conclusions

[37] Between 12 August and 16 September 2000, the CAR onboard the University of Washington Convair CV-580 research aircraft obtained measurements of surface bidirectional reflectance of savanna, salt pans, and stratocumulus clouds throughout southern Africa as part of SAFARI 2000. To measure the BRDF of the surface–atmosphere system, the CV-580 had to bank at a comfortable roll angle of ∼20° and fly in a circle about 3 km in diameter above the surface for roughly 2 min. Multiple circular orbits were acquired over selected surfaces so that average BRDF smoothed out small-scale surface and atmospheric inhomogeneities. In this paper we presented results of BRDFs obtained over two EOS validation sites: Skukuza tower, South Africa (25.0°S, 31.5°E) and Mongu tower, Zambia (15.4°S, 23.3°E). Additional sites are discussed and include the Maun tower, Botswana (20.0°S, 23.5°E), Sua Pan, Botswana (20.6°S, 25.9°E), Etosha Pan, Namibia (19.0°S, 16.0°E) and marine stratus clouds off the west coast of Namibia (20.5°S, 13.1°E). The data presented in this paper have been corrected for atmospheric scattering and absorption using the 6S radiative transfer model.

[38] Results clearly show marked anisotropy in reflected solar radiation over various surfaces types, including savanna, salt pans and marine stratocumulus clouds. The greatest anisotropy in scattered radiation was observed over marine stratus clouds, and was characterized by strong forward scattering as well as water cloud scattering features in the backscattering direction, such as the rainbow and glory. The BRDF over savanna is characterized by a distinct peak in the antisolar direction whose magnitude and location in the principal plane depend on the solar zenith angle. The BRDF also shows distinct directional variations. Over salt pans, the BRDF is more enhanced in the backscattering plane than forward scattering plane and shows little directional variation. The pans show optical characteristics that are suggestive of highly reflecting soil aggregates with very little organic matter.

References

Arnold, G. T., M. D. King, S. C. Tsay, J. Y. Li, and P. F. Soulen, Airborne spectral measurements of surface–atmosphere anisotropy for Arctic sea ice and tundra, *Int. J. Remote Sens.*, *23*, 3763–3781, 2002.

Chandrasekhar, S., *Radiative Transfer*, 393 pp., Dover, Mineola, N. Y., 1960.

Chen, J. M., X. Li, T. Nilson, and A. Strahler, Recent advances in geometrical optical modeling and its applications, *Remote Sens. Rev.*, *18*, 227–262, 2000.

Cihlar, J., D. Manak, and N. Voisin, AVHRR bidirectional reflectance effects and compositing, *Remote Sens. Environ.*, *48*, 77–88, 1994.

d'Entremont, R. P., C. B. Schaaf, and A. H. Strahler, Cloud detection and land surface albedos using visible and near-infrared bidirectional reflectance distribution models, *Proc. 8th Conf. Satell. Meteorol.*, 334–338, 1996.

Dickinson, R. E., B. Pinty, and M. M. Verstraete, Relating surface albedos in GCMs to remotely sensed data, *Agric. For. Meteorol.*, *32*, 109–131, 1990.

DiGirolamo, L., and R. Davies, A band-difference angular signature technique for cirrus cloud detection, *IEEE Trans. Geosci. Remote Sens.*, *32*, 890–896, 1994.

Dubovik, O., and M. D. King, A flexible inversion algorithm for retrieval of aerosol optical properties from Sun and sky radiance measurements, *J. Geophys. Res.*, *105*, 20,673–20,696, 2000.

Dubovik, O., A. Smirnov, B. N. Holben, M. D. King, Y. J. Kaufman, T. F. Eck, and I. Slutsker, Accuracy assessment of aerosol optical properties retrieved from Aerosol Robotic Network (AERONET) Sun and sky radiance measurements, *J. Geophys. Res.*, *105*, 9791–9806, 2000.

Dubovik, O., B. N. Holben, T. F. Eck, A. Smirnov, Y. J. Kaufman, M. D. King, D. Tanré, and I. Slutsker, Variability of absorption and optical properties of key aerosol types observed in worldwide locations, *J. Atmos. Sci.*, *59*, 590–608, 2002.

Gatebe, C. K., M. D. King, S. C. Tsay, Q. Ji, G. T. Arnold, and J. Y. Li, Sensitivity of off-nadir zenith angles to correlation between visible and near-infrared reflectance for use in remote sensing of aerosol over land, *IEEE Trans. Geosci. Remote Sens.*, *39*, 805–819, 2001.

Gutman, G., Normalization of multi-annual global AVHRR reflectance data over land surfaces to common Sun-target-sensor geometry, *Adv. Space Res.*, *14*, 121–124, 1994.

Kaufman, Y. J., The atmospheric effect on remote sensing and its correction, in *Theory and Applications of Optical Remote Sensing*, pp. 336–428, John Wiley, New York, 1989.

Kaufman, Y. J., A. E. Wald, L. A. Remer, B. C. Gao, R. R. Li, and L. Flynn, The MODIS 2.1 μm channel—Correlation with visible reflectance for use in remote sensing of aerosol, *IEEE Trans. Geosci. Remote Sens.*, *35*, 1286–1298, 1997.

Kimes, D. S., P. J. Sellers, and D. J. Diner, Extraction of spectral hemispherical reflectance (albedo) of surface from nadir and directional reflectance data, *Int. J. Remote Sens.*, *8*, 1727–1746, 1987.

King, M. D., A method for determining the single scattering albedo of clouds through observation of the internal scattered radiation field, *J. Atmos. Sci.*, *38*, 2031–2044, 1981.

King, M. D., Directional and spectral reflectance of the Kuwait oil-fire smoke, *J. Geophys. Res.*, *97*, 14,545–14,549, 1992.

King, M. D., M. G. Strange, P. Leone, and L. R. Blaine, Multiwavelength scanning radiometer for airborne measurements of scattered radiation within clouds, *J. Atmos. Oceanic Technol.*, *3*, 513–522, 1986.

King, M. D., L. F. Radke, and P. V. Hobbs, Determination of the spectral absorption of solar radiation by marine stratocumulus clouds from airborne measurements within clouds, *J. Atmos. Sci.*, *47*, 894–907, 1990.

King, M. D., Y. J. Kaufman, D. Tanré, and T. Nakajima, Remote sensing of aerosols from space: Past, present, and future, *Bull. Am. Meteorol. Soc.*, *80*, 2229–2259, 1999.

King, M. D., S. Platnick, C. C. Moeller, H. E. Revercomb, and D. A. Chu, Remote sensing of smoke, land, and clouds from the NASA ER-2 during SAFARI-2000, *J. Geophys. Res.*, *108*, doi:10.1029/2002JD003207, in press, 2003.

Kustas, W. P., R. D. Jackson, and G. Asrar, Estimating surface energy-balance components from remotely sensed data, in *Theory and Applications of Optical Remote Sensing*, pp. 604–627, John Wiley, New York, 1989.

Lean, J., and P. R. Rowntree, Understanding the sensitivity of a GCM simulation of Amazonian deforestation to the specification of vegetation and soil characteristics, *J. Clim.*, *10*, 1216–1235, 1997.

Leroy, M., J. L. Deuzé, F. M. Bréon, O. Hautecoeur, M. Herman, J. C. Buriez, D. Tanré, S. Bouffiè, P. Chazette, and J. L. Roujean, Retrieval of atmospheric properties and surface bidirectional reflectances over land from POLDER/ADEOS, *J. Geophys. Res.*, *102*, 17,023–17,037, 1997.

Lewis, P., The utility of kernel-driven BRDF models in global BRDF and albedo studies, *Proc. Int. Geosci. Remote Sens. Symp.*, *95*, 1186–1187, 1995.

Lewis, P., M. I. Disney, M. J. Barnsley, and J. P. Muller, Deriving albedo maps for HAPEX-Sahel from ASAS data using kernel-driven BRDF models, *Hydrol. Earth Syst. Sci.*, *3*, 1–13, 1999.

Li, X., and A. H. Strahler, Geometric-optical bidirectional reflectance modeling of the discrete crown vegetation canopy: Effect of crown shape and mutual shadowing, *IEEE Trans. Geosci. Remote Sens.*, *30*, 276–292, 1992.

Li, Z., J. Cihlar, X. Zheng, L. Moreau, and H. Ly, The bidirectional effects of AVHRR measurements over boreal regions, *IEEE Trans. Geosci. Remote Sens.*, *34*, 1308–1322, 1996.

Moody, A., and A. H. Strahler, Characteristics of composited AVHRR data and problems in their classification, *Int. J. Remote Sens.*, *15*, 3473–3491, 1994.

Morisette, J. T., J. L. Privette, C. O. Justice, D. Olson, J. Dwyer, P. Davis, D. Starr, and D. Wickland, The EOS land validation core sites: Background information and current status, *Earth Observer*, *11*, 21–25, Nov/Dec 1999.

Nicodemus, F. E., J. C. Richmond, J. J. Hsia, I. W. Ginsberg, and T. Limperis, Geometric considerations and nomenclature for reflectance, U.S.A. Department of Commerce/National Bureau of Standards, *NBS Monogr.*, *160*, 1–52, 1977.

Nolin, A. W., and S. Liang, Progress in bidirectional reflectance modeling and applications for surface particulate media: Snow and soils, *Remote Sens. Rev.*, *18*, 307–342, 2000.

Platnick, S., S. A. Ackerman, R. A. Frey, and M. D. King, Remote sensing of Namibian marine stratocumulus clouds, paper presented at the 28th International Symposium of Remote Sensing of Environment (ISRSE), Somerset West, South Africa, March 27–31, 2000.

Salomonson, V. V., and W. E. Marlatt, Anisotropic solar reflectance over white sand, snow and stratus clouds, *J. Appl. Meteorol.*, *7*, 475–483, 1968.

Salomonson, V. V., and W. E. Marlatt, Airborne measurements of reflected solar radiation, *Remote Sens. Environ.*, *2*, 1–8, 1971.

Schmid, B., et al., Coordinated airborne, spaceborne, and ground-based measurements of massive, thick aerosol layers during the dry season in Southern Africa, *J. Geophys. Res.*, *108*, doi:10.1029/2002JD002297, in press, 2003.

Scholes, R. J., and S. R. Archer, Tree–grass interactions in savannas, *Annu. Rev. Ecol. Syst.*, *28*, 517–544, 1997.

Sinha, P., P. V. Hobbs, R. J. Yokelson, I. Bertschi, D. R. Blake, I. J. Simpson, S. Gao, T. L. Kirchstetter, and T. Novakov, Emissions of trace gases and particles from savanna fires in southern Africa, *J. Geophys. Res.*, *108*, doi:10.1029/2002JD002325, in press, 2003.

Soulen, P. F., M. D. King, S. C. Tsay, G. T. Arnold, and J. Y. Li, Airborne spectral measurements of surface–atmosphere anisotropy during the SCAR-A, Kuwait oil fire, and TARFOX experiments, *J. Geophys. Res.*, *105*, 10,203–10,218, 2000.

Spinhirne, J. D., and T. Nakajima, Glory of clouds in the near-infrared, *Appl. Opt.*, *33*, 4652–4662, 1994.

Strahler, A. H., J. T. Townshend, D. Muchoney, J. Borak, M. Friedl, S. Gopal, A. Hyman, A. Moody, and E. Lambin, MODIS land cover and land cover change: Algorithm technical basis document, *NASA EOS MODIS Doc.*, version 4.1, 102 pp., 1996a.

Strahler, A. H., W. Wanner, C. B. Schaaf, X. Li, B. Hu, J. P. Muller, P. Lewis, and M. J. Barnsley, MODIS BRDF/albedo product: Algorithm theoretical basis document, *NASA EOS-MODIS Doc. Incl. Update*, version 4.0, 252 pp., 1996b.

Swap, R. J., et al., The southern African regional science initiative (SAFARI 2000): Dry-season field campaign: An overview, *S. Afr. J. Sci.*, *98*, 125–131, 2002.

Tsay, S. C., M. D. King, G. T. Arnold, and J. Y. Li, Airborne spectral measurements of surface anisotropy during SCAR-B, *J. Geophys. Res.*, *103*, 31,943–31,954, 1998.

Tucker, C. J., Red and photographic infrared linear combinations for monitoring vegetation, *Remote Sens. Environ.*, *8*, 127–150, 1979.

van de Hulst, H. C., *Multiple Light Scattering, Tables, Formulas, and Applications*, vol. 1, pp. 76–82, Academic, San Diego, Calif., 1980.

Vermote, E. F., D. Tanré, J. L. Deuzé, M. Herman, and J. J. Morcrette, Second simulation of the satellite signal in the solar spectrum, 6S: An overview, *IEEE Trans. Geosci. Remote Sens.*, *35*, 675–686, 1997.

Wanner, W., X. Li, and A. H. Strahler, On the derivation of kernels for kernel-driven models of bidirectional reflectance, *J. Geophys. Res.*, *100*, 21,077–21,089, 1995.

Wanner, W., A. H. Strahler, B. Hu, P. Lewis, J.-P. Muller, X. Li, C. L. B. Schaaf, and M. J. Barnsley, Global retrieval of bidirectional reflectance and albedo over land from EOS MODIS and MISR data: Theory and algorithm, *J. Geophys. Res.*, *102*, 17,143–17,161, 1997.

Wu, A., Z. Li, and J. Cihlar, Effects of land cover type, greenness, and Sun angle on bidirectional distribution of advanced very high resolution radiometer reflectances, *J. Geophys. Res.*, *100*, 9179–9192, 1995.

————————

G. T. Arnold, L3 Communications—EER Communications Systems, Inc., 3750 Centerview Drive, Chantilly, VA 20151, USA. (arnold@climate.gsfc.nasa.gov)

C. K. Gatebe, Goddard Earth Sciences and Technology Center, University of Maryland Baltimore County, Baltimore, MD 21228-5398, USA. (gatebe@climate.gsfc.nasa.gov)

M. D. King, S. Platnick, and E. F. Vermote, Earth Sciences Directorate, National Aeronautical and Space Administration (NASA), Goddard Space Flight Center, Greenbelt, MD 20771, USA. (michael.d.king@nasa.gov; steven.e.platnick@nasa.gov; eric@kratmos.gsfc.nasa.gov)

B. Schmid, NASA Ames Research Center, Moffett Field, CA 94035-1000, USA. (bschmid@mail.arc.nasa.gov)